

Adjoint Slip Inversion under a Constrained Optimization Framework: Revisiting the 2006 Guerrero Slow Slip Event

J. Tago^{1,*}, V.M. Cruz-Atienza², C. Villafuerte², T. Nishimura³, V. Kostoglodov², J. Real² and Y. Ito³

1. Facultad de Ingeniera, Universidad Nacional Autónoma de México

2. Instituto de Geofísica, Universidad Nacional Autónoma de México

3. Disaster Prevention Research Institute, Kyoto University

June 15, 2020

Keywords: Slow slip inversion, Adjoint method, Guerrero Gap

Abstract

Understanding the fault behavior through geodetic data has an important impact in our assessment of the seismic hazard. To shed light on the aseismic evolution of a fault, we developed a new slip inversion strategy, the ELADIN (ELastostatic ADjoint INversion) method, that uses the adjoint elastostatic equations to efficiently compute the gradient of the cost function. ELADIN is a 2-steps inversion algorithm to better handle the slip constraints. In the first step, it finds the slip that better explain the data without any constraints and the second step refines the solution imposing the slip constraints through a Gradient Projection Method. In order to get a physical plausible slip distribution and to overcome the poor fault illumination due to scarce data, ELADIN reduces the solution space by means of a von Karman autocorrelation function that controls the wavenumber content of the solution. To estimate the resolution, we propose a mobile checkerboard analysis which allows to measure a lower bound resolution over the fault for an expected slip patch size and an specific stations deployment. We test ELADIN with synthetic examples and use it to invert the 2006 Guerrero Slow Slip Event (SSE). The later is one of the most studied mexican SSE that unfortunately was recorded with only 15 stations, so a strong regularization is required. We compared our slip solution with two published slip models and found that our solution preserves the general characteristics observed by the other models such as an updip penetration of the SSE in the Guerrero seismic Gap. Despite this similarity, our resolution analysis indicates that this updip aseismic slip penetration might not be a reliable feature of the 2006 SSE.

Introduction

An elegant and powerful mean to solve geophysical inverse problems is the adjoint method (*AM*). Given an objective function, \mathbb{C} , measuring the difference between data and a model prediction (i.e. a forward problem), to determine the model parameters that minimize \mathbb{C} , the *AM* allows computing efficiently the derivative of \mathbb{C} with respect to the parameters by combining the

*Corresponding author: Facultad de Ingeniera, Circuito Interior S/N, Mexico City, Zip Code 04510, phone: (+52)5556220850, email: josue.tago@gmail.com

29 forward problem and the solution of an adjoint equation (i.e. of an adjoint problem) (Fichtner et al., 2006; Tromp et al., 2005;
30 Tarantola, 1984; Gauthier et al., 1986). Thus, the inverse problem can be solved by using any optimization method that exploits
31 that derivative to find the minimum of \mathcal{C} . The most important advantage of the *AM* is its efficiency to compute the derivative
32 of \mathcal{C} that, in many 3D geophysical inverse problems, is simply unaffordable. The *AM* has been successfully used to solve
33 full-waveform inverse problems in seismology, either to determine the elastic properties of the earth (Tromp et al., 2005; Askan
34 et al., 2007; Fichtner et al., 2010; Krischer et al., 2018) or the kinematic history of earthquake sources (Sánchez-Reyes et al.,
35 2018; Somala et al., 2018). However, to our knowledge no adjoint formulation has been proposed to invert geodetic data yet.

36 The slow secular displacement observed in the Earth's crust may be often explained in terms of the aseismic slip occurring
37 at the contact of tectonic plates. Depending on whether the interplate slip rate is larger than the relative plate motion, the
38 plate interface experiences either a coupling regime (i.e. creeping or full locking) (Simpson et al., 1988) or a slow slip event
39 (SSE) (Dragert et al., 2001). In the first case, the associated deformation could be explained through the backslip formulation
40 (Savage, 1983). In the second, a dislocation may predict the displacement field. In the real Earth, the surface displacement
41 is the summation of all contributions from the interface points experiencing either a coupling regime or a SSE. In the case of
42 intra- or inter-plate active faults where aseismic slip or an earthquake may take place, the same reasoning is valid although an
43 earthquake will produce an instantaneous dislocation followed by a postseismic slow slip relaxation (Ozawa et al., 2011). In the
44 present work, to determine the plate interface aseismic slip history in these terms from continuous GPS (or any other geodetic)
45 measurements, we introduce and solve a constrained optimization problem based on the adjoint elastostatic equations with
46 Tikhonov regularization terms (Calvetti et al., 2000; Asnaashari et al., 2013) and a von Karman autocorrelation function (Mai
47 and Beroza, 2002; Amey et al., 2018). The new method, called ELADIN (ELastostatic ADjoint INversion), simultaneously
48 determines the distribution of the interplate coupling and slow slip from surface displacements.

49 In all previous cases, where the crustal strain field corresponds to a quasi-static seismotectonic process, the surface displace-
50 ment is linearly related to the fault slip. However, determining the slip over an extended buried fault from such displacement
51 remains an ill-posed problem. Underdetermination of the model parameters (i.e. of the slip distribution) arises from the sparse
52 sampling of the displacement field and the rapidly decreasing sensitivity of displacement to slip with distance to the fault (Noc-
53 quet, 2018). One rigorous framework to overcome this problem and to determine the uncertainty of such an inverse problem
54 solution are the Bayesian approaches. The incorporation of prior information through probability density functions (pdf) allows
55 determining the posterior model covariance and pdfs, as well as imposing model restrictions by means of truncated prior pdfs
56 (Tarantola and Valette, 1982; Nocquet, 2018; Minson et al., 2013; Yabuki and Matsu'Ura, 1992; Amey et al., 2018; Nocquet
57 et al., 2014; Nishimura et al., 2004). Although Bayesian approaches are widely used and powerful, one important limitation
58 that most have is the large computational load required to determine stochastically the posterior pdfs and thus the uncertainty
59 of the model parameters.

60 An alternative to solve the elastostatic inverse problem is by introducing model regularizations and physically consistent restric-
61 tions. To prevent unrealistic oscillatory slip distributions the most common regularization approach is to smooth the solution by
62 applying a Laplacian operator (i.e., penalizing the second derivative of the slip) (McCaffrey et al., 2007; Wallace and Beavan,
63 2010; Radiguet et al., 2011). Usually the hyperparameter that controls the strength of the smoothing is chosen subjectively by
64 finding a satisfactory weight between the data fit and the smoothing of the slip distribution. One common strategy to determine
65 the hyperparameter is through an L-curve analysis that looks for an optimal hyperparameter value that keeps the data fitted
66 with the strongest possible regularization (Radiguet et al., 2011). From a statistically approach, the hyperparameter can be
67 determined using objective methods such as Akaike's Bayesian Information criterion (ABIC) (Yabuki and Matsu'Ura, 1992;
68 Miyazaki et al., 2006) or fully Bayesian techniques (Fukuda and Johnson, 2008). Although the Laplacian operator reduces
69 unphysical and rough slip solutions (and thus unreliable large stress drops), this is not the most convenient mathematical strat-
70 egy to preserve the real nature of the slip when regularizing the problem, where the self-similarity of the fault slip observed in
71 earthquakes should be resolved as proposed by Amey et al. (2018).

72 When designing ELADIN, our goal was introducing a regularization approach that preserves the nature of faulting (i.e. the slip
73 self-similarity) and, at the same time, that allows a spectral control of the problem solution that guaranties a given resolution
74 criterion. To this purpose we introduce a von Karman autocorrelation function that reduces the solution space to a domain where
75 the wavenumber content of all possible solutions satisfies a minimum characteristic length previously determined through ro-
76 bust resolution tests. We illustrate the capabilities of the method by inverting GPS data for the 2006 Guerrero SSE, which has
77 been widely investigated in the literature, and describe several benefits that our solution has as compared with some previous
78 models.

79 Systematic inversion of real GPS data along the Mexican subduction zone applying the ELADIN method is presented in an
80 associated work (Cruz-Atienza et al., 2020) where we analyzed the aseismic slip history between 2017 and 2019.

81 **The ELADIN Method**

82 In this section, we first introduce the forward model that allow us to compute the synthetic displacements produced by a slip
83 over the fault. Then, we formulate the inverse problem in a constrained optimization framework, reducing the solution space
84 to control its spectral content with a von Karman correlation function. We also include a Tikhonov term to penalize regions
85 where slip is not expected to occur and slip magnitude constraints. Finally, we present a 2-step algorithm that first solves the
86 inverse problem without slip constraints using the adjoint equations for the gradient computation. Then we project the resulting
87 solution into the feasible solution space to initiate the second step by following the Gradient Projection method to optimize the
88 solution by respecting the desired slip constraints.

89 Forward model

90 The representation theorem for the elastostatic equations models the displacement, $\underline{u}(\underline{x})$, due to a slip, $\underline{d}(\underline{\xi})$, produced at a fault,
91 Σ , as

$$u_j(\underline{x}) = \int_{\Sigma} T_k(S_{ij}(\underline{\xi}, \underline{x}), \hat{n}(\underline{\xi})) d_k(\underline{\xi}) d\Sigma, \quad i, j, k \in \{x, y, z\}, \quad (1)$$

92 where $T_i(\cdot, \cdot)$ is the i -component of the traction on the fault computed through the Somigliana tensor, $S_{ij}(\underline{\xi}, \underline{x})$, and the fault
93 normal vector $\hat{n}(\underline{\xi})$. If the traction and the slip are projected along the plate convergence, c -, and the complementary perpen-
94 dicular, p -direction, eq. (1) can be written in matrix form as

$$\begin{aligned} \begin{bmatrix} u_1(\underline{x}) \\ u_2(\underline{x}) \\ u_3(\underline{x}) \end{bmatrix} &= \int_{\Sigma} \begin{bmatrix} T_p(S_{i1}(\underline{\xi}, \underline{x}), \hat{n}(\underline{\xi})) & T_c(S_{i1}(\underline{\xi}, \underline{x}), \hat{n}(\underline{\xi})) \\ T_p(S_{i2}(\underline{\xi}, \underline{x}), \hat{n}(\underline{\xi})) & T_c(S_{i2}(\underline{\xi}, \underline{x}), \hat{n}(\underline{\xi})) \\ T_p(S_{i3}(\underline{\xi}, \underline{x}), \hat{n}(\underline{\xi})) & T_c(S_{i3}(\underline{\xi}, \underline{x}), \hat{n}(\underline{\xi})) \end{bmatrix} \begin{bmatrix} d_p(\underline{\xi}) \\ d_c(\underline{\xi}) \end{bmatrix} d\Sigma, \quad i \in \{x, y, z\} \\ \underline{u}(\underline{x}) &= \int_{\Sigma} \underline{T}(\underline{\xi}; \underline{x}) \underline{d}(\underline{\xi}) d\Sigma. \end{aligned} \quad (2)$$

95 Then, the fault is discretized in M subfaults such that the integral can be approximated as

$$\underline{u}(\underline{x}) \simeq \sum_{i=1}^{M \text{ subfaults}} A^i \underline{T}(\underline{\xi}^i; \underline{x}) \underline{d}(\underline{\xi}^i), \quad (3)$$

96 where A^i is the i -subfault area. Finally, if we want to compute the displacement for N receivers, we can order the displacements
97 in a single vector such that the entire computation is reduced to a simple matrix-vector product as

$$\begin{aligned} \begin{bmatrix} \underline{u}(\underline{x}^1) \\ \underline{u}(\underline{x}^2) \\ \vdots \\ \underline{u}(\underline{x}^N) \end{bmatrix} &= \begin{bmatrix} A^1 \underline{T}(\underline{\xi}^1; \underline{x}^1) & A^2 \underline{T}(\underline{\xi}^2; \underline{x}^1) & \cdots & A^M \underline{T}(\underline{\xi}^M; \underline{x}^1) \\ A^1 \underline{T}(\underline{\xi}^1; \underline{x}^2) & A^2 \underline{T}(\underline{\xi}^2; \underline{x}^2) & \cdots & A^M \underline{T}(\underline{\xi}^M; \underline{x}^2) \\ \vdots & \vdots & \ddots & \vdots \\ A^1 \underline{T}(\underline{\xi}^1; \underline{x}^N) & A^2 \underline{T}(\underline{\xi}^2; \underline{x}^N) & \cdots & A^M \underline{T}(\underline{\xi}^M; \underline{x}^N) \end{bmatrix} \begin{bmatrix} \underline{d}(\underline{\xi}^1) \\ \underline{d}(\underline{\xi}^2) \\ \vdots \\ \underline{d}(\underline{\xi}^M) \end{bmatrix}, \\ \underline{U} &= \underline{T} \underline{D}, \end{aligned} \quad (4)$$

98 where $\underline{U} \in \mathbb{R}^{3N}$, $\underline{T} \in \mathbb{R}^{3N \cdot 2M}$ and $\underline{D} \in \mathbb{R}^{2M}$.

99 Inverse problem

100 The inverse problem consists in recover the slip at each subfault of a known interface that produces displacements observed
101 at geodetic stations. Due to the linearity of the forward model, eq. (4), we construct a quadratic cost function to formulate a
102 convex inverse problem as

$$\mathbb{C}(\underline{D}) = \frac{1}{2} [\underline{U} - \underline{U}_o]^T [\underline{U} - \underline{U}_o], \quad \text{s.t.} \quad \underline{U} = \underline{T} \underline{D}, \quad (5)$$

103 where $\underline{U}_o \in \mathbb{R}^{3N}$ are the displacements observed at the N geodetic stations stored in a single ordered vector, as we did with \underline{U}
 104 in eq. (4). Unfortunately, for real data due to its sparse coverage and its noise content, the inverse problem (5) is ill-conditioned.
 105 In order to solve this issue, regularization and realistic physical constraints will be introduced.

106 **Regularization: von Karman correlation function**

107 Most of the time, the regularization is done with two elements a model precision matrix and/or with Tikhonov terms. The model
 108 precision matrix is the inverse of the model covariance matrix which for our case controls how sensitive are each subfaults slip
 109 to its neighbours slip. Radiguet et al. (2011) propose a subfault correlation that follows a decreasing exponential function
 110 according to a defined correlation length. The problem encountered is that the precision matrix for different correlation lengths
 111 does not have a different effect due to the fast decay of this correlation. For different type of correlation functions, the model
 112 covariance matrix starts to become ill conditioned when the subfaults length becomes smaller than the correlation length.

113 The use of a Tikhonov term in the cost function is to penalize the roughness of the solution. Generally, the penalization is done
 114 to the first or second derivatives of the solution. However, when we penalize the derivatives usually the norm of the solution is
 115 also reduced. Besides, these two alternatives involve hyperparameters that need to be optimally computed since they control de
 116 trade off between the misfit of the data and the size of the regularization solution.

117 These inconveniences lead us to propose to reduce the solution space whose wavenumber content, minimum slip patches size,
 118 can be controlled. The main idea is to apply a filter operator, \underline{F} , to the slip \underline{D} . Then the inverse problem (2) can be formulated
 119 as

$$\mathbb{C}(\underline{D}) = \frac{1}{2} [\underline{U} - \underline{U}_o]^T \underline{C}_d^{-1} [\underline{U} - \underline{U}_o], \quad \text{s.t.} \quad \underline{U} = \underline{TF}, \underline{D} \quad (6)$$

120 where \underline{C}_d is the data covariance matrix to weight the data according to its quality or importance.

121 Recently, Amey et al. (2018) showed that a von Karman regularization for slip inversions is a good strategy to introduce the
 122 slip self-similar properties that can not be achieved with a common Laplace regularization. The spatial von Karman correlation
 123 function is

$$vk(r) = \frac{r^H K_H(r)}{(1e^{-10})^H K_H(1e^{-10})}, \quad (7)$$

124 where H is the Hurst exponent, $K_H(\cdot)$ is the modified Bessel function of second kind of order H , r is the correlation length
 125 that can be computed as

$$r = \sqrt{\frac{s^2}{a_s^2} + \frac{d^2}{a_d^2}}, \quad (8)$$

126 where (s, d) are the coordinates along strike- and dip-directions on the fault and (a_s, a_d) are the correlation lengths along
 127 strike- and dip-directions, respectively. This correlation function can be used to construct a linear operator K , which convolved

128 with the slip D can control its wavenumber content along strike and dip component. This convolution can be formulated as a
 129 matrix-vector product where the matrix operator, \underline{E} , applies the convolution of the linear operator K to the slip, \underline{D} , as it is in
 130 eq. (6).

131 Slip constraints

132 The regularization guarantee that an optimal slip can be found, however this solution may not have physical sense. Slip
 133 constraints need to be imposed according to physical hypothesis and available information. Such that, the inverse problem (6)
 134 can be reformulated as

$$\mathbb{C}(\underline{D}) = \frac{1}{2} [\underline{U} - \underline{U}_o]^T \underline{C}_d^{-1} [\underline{U} - \underline{U}_o] + \frac{\beta}{2} [\underline{W}(\underline{E}\underline{D} - \underline{D}_p)]^T [\underline{W}(\underline{E}\underline{D} - \underline{D}_p)], \quad (9)$$

s.t.

$$\underline{U} = \underline{T}\underline{E}\underline{D}, \quad (10)$$

$$D_i^{j,l} \leq (\underline{E}\underline{D})_i \leq D_i^{j,u}, \quad i \in \{p, c\} \wedge j \in \{\text{SSE, Coupling}\} \text{ regime}, \quad (11)$$

135 where β is a hyperparameter, \underline{W} is a diagonal model weight matrix that penalizes the slip per subfaults, \underline{D}_p is an *a priori* slip
 136 solution and $(D_i^{j,l}, D_i^{j,u})$ are the lower and upper limits of the i -component of the slip in the j -regime. The slip is in the SSE
 137 regime if its c -component is contrary to the convergence direction and it is in the coupling regime otherwise. If we have an
 138 *a priori* slip solution, \underline{D}_p , we can force our solution to be as close as possible to it, only allowing changes when the match
 139 with the observations is improved. In that case, the weight matrix should be the identity matrix, $\underline{W} = \underline{I}$. On the other hand,
 140 when we lack off a previous solution, we impose $\underline{D}_p = 0$ and to get the minimum norm solution we make again $\underline{W} = \underline{I}$. In
 141 this study, we are not interested in getting the minimum norm solution, so we set $\underline{W} = 0$ everywhere except for the subfaults
 142 where we believe there must be free slip (i.e. no coupling or SSE regime). The bigger the value is assigned, the bigger subfault
 143 penalization to slip. The hyperparameter β controls the trade off between the fit of the data and the slip constraints imposed in
 144 the cost function. However, since it is used with the penalization term to prevent slip, its value should only guarantee that we do
 145 not observe slip in those penalized regions. However, if an *a priori* slip solution, $(\underline{D}_p \neq 0, \underline{W} = \underline{I})$ is used or a minimal norm
 146 solution $(\underline{D}_p \neq 0, \underline{W} = \underline{I})$, its value must be computed following an optimal strategy as an L-curve analysis (e.g. Radiguet
 147 et al. (2011)) or the ABIC criterion (e.g. Miyazaki et al. (2006)).

148 Gradient computation: Adjoint method

149 To solve the inequality-constrained inverse problem (6), first we consider how to compute the gradient of the cost function
 150 without considering the inequality constraints, eq. (11). In the framework of constrained inverse problems, the Lagrangian can
 151 be computed as

$$\mathcal{L}(\underline{D}, \underline{U}, \lambda) = \mathbb{C}(\underline{D}) + \lambda^T [\underline{U} - \underline{T}\underline{E}\underline{D}], \quad (12)$$

152 where $\underline{\lambda}$ are the Lagrange multipliers. The Lagrangian total derivative with respect to the slip, \underline{D} , is

$$D_{\underline{D}}\mathcal{L} = \nabla_{\underline{D}}\mathcal{L} + \nabla_{\underline{U}}\mathcal{L} \cdot \nabla_{\underline{D}}\underline{U} + \nabla_{\underline{\lambda}}\mathcal{L} \cdot \nabla_{\underline{D}}\underline{\lambda}, \quad (13)$$

153 To simplify the computation of the gradient, we follow the adjoint method strategy (Fichtner et al., 2006). We start forcing
 154 $\nabla_{\underline{\lambda}}\mathcal{L} = 0$ by solving a forward model $\tilde{\underline{U}} = \underline{\mathcal{T}}\underline{F}\underline{D}$. Then, we use the modeled displacements, $\tilde{\underline{U}}$, to compute the adjoint source
 155 as $\tilde{\underline{\lambda}} = \underline{C}_d^{-1} [\underline{U}_o - \tilde{\underline{U}}]$ which implies $\nabla_{\underline{U}}\mathcal{L} = 0$. Such that the Lagrangian total derivative is the solution of the adjoint problem
 156 plus a term related with the slip constraints as

$$\begin{aligned} D_{\underline{D}}\mathcal{L} &= \nabla_{\underline{D}}\mathcal{L} \\ &= -(\underline{\mathcal{T}}\underline{F})^T \tilde{\underline{\lambda}} + \beta \left[\underline{F}^T \underline{W}^T \underline{W} (\underline{F}\underline{D} - \underline{D}_p) \right]. \end{aligned} \quad (14)$$

157 With the gradient evaluated we can follow any numerical optimization strategy to find the minimum solution.

158 Gradient Projection Method

159 To avoid dealing with inequality constraints, it is often convenient to project the solution into the physically-consistent space
 160 after each iteration of the inversion procedure. However, we realized that for the slip inversion this projection is not convenient
 161 because frequently the gradient direction is orthogonal to the slip constraints making the algorithm to stop. For large scale
 162 problems and with lower and upper bounds for the variables, Nocedal and Wright (2006) propose the Gradient Projection
 163 Method (GPM) as an efficient strategy to deal with inequality restrictions. The GPM consists of two stages per iteration. In
 164 the first stage, the steepest descent direction is followed until a bound is encountered which needs to be bent to stay feasible.
 165 Then along the resulting piecewise-linear path, a local minimizer, called *Cauchy point*, is found (see Appendix A for details).
 166 For the second stage, a new optimum point is searched in the face of the feasible box on which the Cauchy point lies, i.e. those
 167 slip constraints that have reached a limit are changed to equality constraints. It implies that those inequality constraints now are
 168 part of the active set. This subproblem is usually not solved exactly but the remaining inequality constraints are respected.

169 For the slip inversion we do not follow exactly the GPM to avoid the subproblem of the second stage. So, after computing the
 170 Cauchy point, we take it as a new iteration point where the gradient is computed again. Thus, it is essentially a steepest descent
 171 algorithm that respects the inequality constraints. Our GPM version is slow so to achieve a fast convergence, we then propose
 172 an algorithm that is explained in the next section.

173 2-step inversion algorithm

174 In order to increase the convergence speed, we developed a 2-step inversion algorithm. The purpose of the first step is to get
 175 an optimal initial solution for the GPM. In this step we solve the unconstrained slip inverse problem using the adjoint method

176 to compute the gradient. With the gradient any iterative optimization algorithm can be used, e.g. Conjugate Gradient method,
 177 1-BFGS method, etc. In this work, we use the SEISCOPE optimization toolbox, which is a friendly and powerful optimization
 178 library developed in FORTRAN 90 with many optimization strategies to choose from (Métivier and Brossier, 2016). In the
 179 second step, the constrained slip inverse problem is solved with a slight modification of the GPM. Since after computing the
 180 Cauchy point, instead of reformulating the inverse problem according to the new active set incorporating some inequality
 181 constraints, we use it as the new iteration of the slip. This is not as fast as solving the traditional GPM, but since we are close
 182 to the optimal solution few iterations are needed. The pseudocode is described in the Algorithm .

Algorithm 1: 2-Steps Algorithm

1st Step: Unconstrained slip inverse problem (Adjoint method)

Data: GPS Data

Initialize the slip $\underline{D}_0 = 0$;

while Convergence is not achieved **do**

1. Compute a forward problem

$$\underline{U}_k = \underline{T}\underline{E}\underline{D}_k.$$

2. Compute the adjoint source

$$\underline{\lambda}_k = \underline{C}_d^{-1} [\underline{U}_o - \underline{U}_k].$$

3. Compute the adjoint problem to get the gradient

$$\nabla_{\underline{D}} \mathcal{L} = -(\underline{T}\underline{E})^T \underline{\lambda}_k + \beta \left[\underline{E}^T \underline{W}^T \underline{W} (\underline{E}\underline{D}_k - \underline{D}_p) \right]$$

183 4. With the gradient use any iterative optimization algorithm to find an update step $\Delta \underline{D}_k$

5. Update the slip

$$\underline{D}_{k+1} = \underline{D}_k + \Delta \underline{D}_k.$$

end

2nd Step: Constrained slip inverse problem (Gradient Projection Method)

Data: Optimal solution of 1st step, \underline{D}^*

Project \underline{D}^* into the feasible region to get the initial solution \underline{D}_0 ;

while Convergence is not achieved **do**

1. From \underline{D}_k compute the Cauchy point \underline{D}_k^c (details in Appendix A)

2. Update the slip

$$\underline{D}_{k+1} = \underline{D}_k^c.$$

end

184 Resolution

185 Resolution of our inverse problem essentially depends on the geometry configuration of the problem. This is, on the fault
 186 geometry and the distribution of observation sites (i.e. on the displacement field sampling and the sensitivity of displacement
 187 to dislocations in the fault). For a given problem discretization and slip pattern, synthetic inversions are a powerful mean to
 188 quantify how well an inverse method performs. If well-conceived, these tests may lead to very useful resolution information
 189 under realistic conditions (i.e. if they include data uncertainties and minimize the dependence on the target model). In the
 190 following, we present comprehensive exercises where the restitution of the target model is systematically quantified. To this
 191 purpose, for a given solution we define the restitution index, r_i as

$$r_i = 1 - \left| \frac{d_i^T - d_i^I}{d_i^T} \right|, \quad (15)$$

192 where d_i^T and d_i^I are the slip for the target and inverted models of the i -subfault. The slip used for the restitution index can
 193 be along the plate convergence or its perpendicular direction. Furthermore, the average restitution index, ari , is the mean
 194 restitution index over the M subfaults that discretize the 3D subduction interface between the Cocos and the North American
 195 plates in central Mexico (Cruz-Atienza et al., 2020). r_i is one if the inverted slip equals the target slip and zero if the difference
 196 between them equals the target value. We have discretized the plate interface with subfaults whose surface surface projection
 197 is a square of $10 \times 10 \text{ km}^2$ and assumed a four-layer 1D structure suitable for the region (Campillo et al., 1996). For the
 198 analysis, we have considered all available permanent GPS stations (66 sites) in central Mexico (Cruz-Atienza et al., 2020;
 199 CruzAtienza et al., 2018) and 5 ocean bottom pressure gauges (OBP) deployed in the Guerrero seismic gap since November
 200 2017 (CruzAtienza et al., 2018), where only the vertical displacements were considered.

201 Mobile checkerboard

202 A widely used strategy to quantify an inverse problem resolution is the checkerboard (CB) test. However, this test is intrinsically
 203 linked to the arbitrary choice of the target CB model, which means to the CB unit size, its positions in space and the absolute
 204 model-properties periodically attributed. For this reason, we performed comprehensive mobile checkerboard (MOC) tests for
 205 different patch sizes (PS). Based on previous GPS data inversions in central Mexico (Radiguet et al., 2012; Cruz-Atienza et al.,
 206 2020), we attributed patch slip values in the plate convergence direction of 30 cm (i.e. as typical SSEs in the region) and -10
 207 cm (i.e. a backslip corresponding to 20 months of full coupling assuming a 6 cm/y plate convergence rate).

208 Figure 1 shows the inversion results for three CBs with different PS (i.e. 60, 80 and 100 km) and the same correlation length
 209 (i.e. $L = 20 \text{ km}$). As well see next, this value of L maximizes the average restitution index (ari) in these cases where no slip
 210 restriction was imposed (i.e. no gradient projection method was used) and no data uncertainly was considered (i.e. the precision
 211 matrix is the identity matrix). Although the data fit is almost perfect in all three cases, it is clear that the target model restitution

212 strongly depends on PS, the slip model characteristic length. As expected, the larger PS the better is the restitution. This is
 213 quantified in the right column, where the restitution index, r , is displayed for all subfaults. Besides, two more conclusions
 214 stand out: (1) restitution is better in SSE patches than in coupling patches, and (2) the inversion scheme cannot resolve the
 215 unrealistic slip discontinuity along the boundary of the CB patches. Both conclusions were expected because the backslip is
 216 one third of the positive slip, and because of both the imposed model regularization and the limited sensitivity of displacements
 217 with distance to the fault.

218 Previous results do not provide a reliable estimate of the problem resolution when facing real data because in that case we do not
 219 know the actual slip producing the observed displacements. A MOC test consists in multiple CB inversions so that all possible
 220 model positions are explored. Results from the test may be translated into the mobile checkerboard restitution index ($mcri$) per
 221 subfault, which corresponds to the average of the r values estimated for each inversion. The $mcri$ is a quantity that eliminates
 222 the resolution dependence on the CB position. For a given PS, we performed 6 MOC tests, one without regularization (i.e. L
 223 = 0 km) and the rest with different correlation lengths (i.e. for $L = 10, 20, 30, 40$ and 50 km). Five different PS of 40, 60, 80,
 224 100 and 120 km were considered and each one required different number of CB inversions. Since we discretized the fault with
 225 projections of side length $h = 10$ km, we move the checkerboard along the dip and strike directions with a jump of 2 km until
 226 we covered all the possible configurations. The total number of CB test for an specific PS per value of L can be computed as
 227 $(PS/10)^2$.

228 Figure 2 presents an overview of three MOC tests for PS of 60, 80 and 100 km (i.e. those considered in Figure 1). As expected,
 229 in the top row we see that the $mcri$ increases with the PS, reaching values close to 0.8 in some regions close to the coast where
 230 there is the largest density of stations, and where the plate interface is closest to them. In deeper interface regions, between 30
 231 and 50 km depth, $mcri$ falls down up to about 0.2 for PS of 60 km and over 0.5 for PS of 100 km along the whole subductions
 232 zone. As clearly seen in the right column of Figure 1, the unrealistic slip discontinuities along the patches edges strongly
 233 difficults the restitution, so we can considerer the $mcri$ maps of Figure 2 (first row) as a lower resolution bound. Isocontours
 234 of these maps for different PSs and optimum correlation lengths thus define reliable fault regions where the inversions should
 235 resolve the unknown target slip above the $mcri$ isocontour value (e.g., above 40% of the target slip if $mcri$ equals 0.4).

236 The MOC tests allow to identify the optimum correlation length per subfault that maximizes the ari. This is shown in the second
 237 row of Figure 2, where we see that L decreases for PS of 100 km along the coast as compared with smaller slip characteristic
 238 lengths (i.e. for smaller PSs). The opposite happens in deep and less instrumented interface regions, where L increases with
 239 PS. Notice also that regularization should be stronger offshore, close to the subduction trench, as PS decreases. Based on this
 240 multiscale analysis we assembled optimum solutions for the same CBs of Figure 1 by integrating the best inverted slip per
 241 subfault (i.e. for the optimum local regularization). Resolution improvements for the multiscale models ranged between 10%
 242 and 20% as shown in the third row of the figure (compare with the right column of Figure 1). However, something unexpected

243 came out when comparing whole-interface average *mcri* values for all MOC tests. Figure 3 shows this metric along with the
 244 average data-misfit error (i.e. the L2 norm of the difference between target and inverted displacements) for all tested PSs as
 245 a function of L, the correlation length. Although the spatial distribution of the optimum L depends on the slip characteristic
 246 length PS, the best average regularization was the same for all PSs and equal to 20 km. Such independency of the average
 247 *mcri* on L for different PSs is due that the jump in the checkerboards will pass everywhere in the subfault no matter the PS
 248 (the number of CB increases with a bigger PS selection). Besides, as explained below, another factor related with this result,
 249 arises from the absence of noise (uncertainty) in the inverted data and model restrictions (no GPM). What is remarkable and
 250 was expected in Figure 3 is that (1) the models restitution shows a concave behavior with the slip characteristic length and (2)
 251 the best fitting models are not the best solutions. Regularization is critical to achieve physically acceptable and reliable slip
 252 models.

253 **Gaussian slip**

254 The analysis of the previous section did not consider the uncertainty in geodetic measurements that may be significantly large,
 255 especially in the vertical component where meteorological noise and non-tectonic physical signals are present. Nor did the
 256 analysis incorporate slip restrictions that are essential to guaranty tectonic expectations in our solutions such as smaller-than-
 257 expected backslip for full interface coupling and slip rake angles near the plate convergence direction. For this reason, we now
 258 analyze three new synthetic cases where (1) the target slip corresponds to truncated Gaussian slip distributions (i.e. to an SSE)
 259 surrounded by a full-coupled plate interface, and (2) the associated surface displacements (i.e. the inverted data) are strongly
 260 and randomly perturbed according to a normal probability distribution given by the data covariance per component, which we
 261 took as 2.1, 2.5 and 5.1 mm in the north, east and vertical directions, respectively (Radiguet et al., 2011).

262 Figure 4 shows the target slip models and both, the associated exact displacements (blue arrows) and the perturbed ones (red
 263 arrows). The data uncertainty is represented by the gray ellipses at the tips of the perturbed vectors, the semiaxes corresponding
 264 to the standard deviation of the normal distribution used to perturb the data per component. The interplate coupling corresponds
 265 to three-months cumulative backslip assuming a 6 cm/yr plate convergence (i.e. 1.5 cm), and the geometry and position of the
 266 three Gaussian slip patches were inspired by recent SSE solutions found in the region (Cruz-Atienza et al., 2020). Please notice
 267 how large are the perturbations.

268 Inversions for the three Gaussian slip models were done for both the exact and perturbed data. Each set of data was inverted
 269 without regularization and with correlation lengths of 10, 20, 30, 40, 50 and 60 km. In all cases backslip restrictions were applied
 270 by means of the GPM so the interplate coupling could never overcome the value of one. Figure 5A shows some slip solutions
 271 for the largest-Gaussian exact data along with the associated restitution maps. Although the data fit is excellent in all cases,
 272 acceptable solutions are only retrieved when model regularization is applied. For L = 30 km, the *ari* is above 0.9 so that the slip
 273 solution is almost perfect, except along the Gaussian contour where there is an unrealistic slip discontinuity in the target model

274 (i.e. a similar problem as for the checkerboards of last section).

275 When random noise is added to the observations and the inverse problem is solved by integrating the data uncertainty by means
276 of the precision matrix, the model regularization becomes even more critical to achieve a good solution. This can be seen in
277 Figure 5B, where the restitution is very poor around the Gaussian slip when no regularization is applied as compared with that
278 for $L = 40$ km, for which the ari is also above 0.9 and the slip solution is surprisingly good. Also surprising, results for the
279 other two smaller Gaussian models were very similar (see Appendix B, Figures S1 and S2). A summary of the 42 inversions
280 (i.e. 14 per Gaussian model) is shown in Figure 6, where we see that although the data-fitting errors for the noisy inversions
281 are roughly four times larger than those obtained from the exact data, the ari in all cases is above 0.9 for the best solutions (i.e.
282 for the optimum L) even for the smallest and circular Gaussian case, which has a slip characteristic length smaller than 80 km
283 centered at 38 km depth.

284 **The 2006 Guerrero SSE**

285 During the 20 years preceding the devastating 2017 Mw8.2 Tehuantepec earthquake that took place offshore the Oaxaca state,
286 Mexico, long term SSEs in Guerrero occurred almost every four years (i.e. six events between 1998 and 2017) and had a
287 remarkably large moment magnitudes ($M_w > 7.5$) (Kostoglodov et al., 2003; Radiguet et al., 2012; CruzAtienza et al., 2018).
288 After the earthquake, the regional plate-interface SSE beating has strongly changed so that two other SSEs took place in
289 that state in the next two years (in 2018 and 2019) with much smaller magnitudes (M_w around 7.0) (Cruz-Atienza et al.,
290 2020). The 2006 Guerrero SSE has been the most investigated event in Mexico despite the poor GPS instrumentation on that
291 time (Kostoglodov et al., 2010; Vergnolle et al., 2010; Radiguet et al., 2011, 2012; Cavali et al., 2013; Bekaert et al., 2015;
292 Villafuerte and Cruz-Atienza, 2017). One of its most interesting features is that, unlike adjacent subduction segments, the slow
293 slip penetrated the seismogenic updip region of the plate interface up to 15 km depth in the Guerrero seismic gap. In this
294 section we perform a thorough analysis of the inverse problem resolution for that event and provide what we think are its most
295 reliable features as compared with previous results reported in the literature.

296 **Resolution**

297 In previous sections we found that the problem resolution depends on two main parameters: (1) the slip characteristic length
298 (PS) and (2) the inverse-problem correlation length (L). This is true for a given problem geometry (i.e. for a stations array and
299 plate interface geometry). For this reason, we can determine fault regions where resolution (i.e. the restitution index) is high
300 enough for a given L , which means that the inverted slip in those regions is valid within the wavenumber bandwidth associated
301 to the von Karman spectrum for that L . Since only 12 GPS sites registered the 2006 SSE, we performed three different MOC
302 tests considering only the location of these sites. The tests were done for checkerboard unit lengths (PS) of 80, 100 and 120

303 km, and for $L = 0$ (no regularization), 10, 20, 30, 40, 50 and 60 km. This resolution exercise required multiple CB inversions
304 for each PS choice, as explained before, where reasonable backslip and rake angle restrictions were imposed using the GPM.
305 The slip lower limit was the negative slip patch value imposed, -8 cm, and the rake angle is restricted to the $[20, -20]^\circ$ range.

306 Plate-interface resolution maps (i.e. for the mcric metric) are shown in Figure 7 as a function of PS and L. As expected, overall
307 mcric values increase with PS for a given L. Similarly, they also increase with L for a given PS. However, supplementary figures
308 not show here reveal that, in the latter case, the high-resolution regions stop expanding for L above 30 km for all three PS cases.
309 The maps show isocontours for mcric = 0.6, which delineate fault regions where the slip solutions are likely to resolve the actual
310 slip within 40% error. As explained previously, these maps represent a lower resolution bound because the MOC tests assume
311 unrealistically sharp slip discontinuities that strongly penalize the restitution index due to the boundaries of the square slip
312 patches (e.g. see Figure 1). For this reason, we expect the resolution within the regions to be higher than the mcric isocontours
313 value. Either way, even in the MOC test for the maximum PS and L values, the high resolution region does not extend across
314 the whole expected SSE area, as claimed by previous authors using different inversion techniques (Radiguet et al., 2011). Our
315 resolutions maps represent the key piece allowing us to tell something reliable (to some point) about the 2006 SSE.

316 Figure 8 summarizes the results from all MOC tests in terms of the average mcric and data-misfit L2 error. Although errors
317 are similar for all slip characteristic lengths PS, average mcric values follow a concave trajectory with L as previously noticed
318 from Figure 7. However, unlike the previous MOC exercises for all currently available geodetic stations (Figures 2 and 3),
319 the optimum correlation lengths (i.e. those maximizing the restitution) increase with PS. This is not clear for PS = 120 km,
320 however it shows a flatter function after the optimum and we expect the optimal L should be in the (20,30) km range. This
321 remarkable and reasonable result is due to both the slip restrictions and the sparse stations array. It tells us that, depending on
322 the characteristic SSE-patch-size we want to solve the best, the problem regularization should be adapted. For instance, if we
323 are interested in SSE patches with a characteristic length of 80 km, then $L = 10$ km is the optimum choice. Of course, such
324 small value is detrimental to the extent of the acceptable resolution region, as seen in Figure 7. If $L = 20$ km, then patches with
325 characteristic length of 100 km will be optimally solved in a larger fault region.

326 **2006 SSE Inversions**

327 The inversions we present next were done using the same GPS data as Radiguet et al. (2011). . This means that the displacement
328 timeseries were carefully pre-processed (Vergnolle et al., 2010) and then corrected from inter-SSE long-term deformations by
329 subtracting the linear trends from the period 2003-2005 per station. The resulting time series thus show the deviations from the
330 long-term steady motion during the 2006 Guerrero SSE.

331 Since the long-term displacement trends per station are significantly different in Guerrero (Radiguet et al., 2012), By removing
332 the secular deformation patterns, we are implicitly eliminating the common reference frame given by the North American plate,

333 which also leads to a possible overestimation of the SSE-induced displacements. Either way, for the sake of comparison with
 334 previous solutions using this dataset, we have inverted the timeseries from January 30 (2006) to January 15 (2007) for four
 335 different correlation lengths ($L = 10, 20, 30$ and 40 km) and slip restrictions (i.e. applying the GPM), so that the backslip could
 336 not overcome the full-coupling regime in that period and the rake vector could vary $\pm 20^\circ$ from the plate-convergence (pc)
 337 direction.

338 Figure 9 shows the inversion results for two optimal correlation lengths ($L = 20$ and 30 km). Since the data is almost perfectly
 339 explained in both cases, the preferred solution will depend on both the scale at which we are interested in for interpretations and
 340 reasonable physical considerations. Taking the 1 cm slip contour as the effective SSE area, then the moment magnitude of the
 341 2006 event is consistent for both inversions and equal to $M_w 7.4$. For estimating M_w , we considered a typical crustal rigidity
 342 $\mu = 32 \times 10^9$ Pa.

343 As shown in the last section, given the poor GPS coverage during the 2006 SSE, the inverse problem regularization plays a
 344 critical role to have some confidence in what the slip solutions tell us. In the absence of resolution analysis, it is difficult to
 345 justify any conclusion, especially between distant stations. For instance, the absence of data along most of the north-west
 346 Guerrero seismic gap (NW-GGgap) (i.e. between ZIHP and CAYA) (UNAM, 2015) and the Guerrero Costa Chica (i.e. between
 347 CPDP and PINO) is unfortunate and obliges us to be cautious in the interpretations. Previous investigations concluded that
 348 SSEs behave differently between these two Guerrero subduction segments so that, unlike the Costa Chica, the slow slip in the
 349 NW-GGgap reaches the seismogenic interface zone (i.e. up to 15 km depth) (Radiguet et al., 2011; Cavali et al., 2013) releasing
 350 aseismically a significant part of the accumulated inter-SSE strain (Radiguet et al., 2012; Bekaert et al., 2015).

351 Figure 10 shows a comparison between our preferred solution (model A) (i.e. for $L = 30$ km) and two previously published
 352 solutions, one from the simultaneous inversion of both GPS and InSAR data (Model B / (Cavali et al., 2013)) and the other from
 353 GPS data only (model C / Radiguet et al. (2011)). Our solution is show together with the associated 60% resolution regions
 354 (regions where the average m_{cri} is higher than 0.6), which are taken from Figure 7 according to the optimal solutions of Figure
 355 8. Confidence contours delineate the fault regions where solutions disagree with the actual slip by less than 40% in different
 356 wavenumber bandwidths depending on L . The red contour delineate the 60% confidence regions for a slip characteristic length
 357 of 80 km and the green one for a 120 km characteristic length. Although the three slip solutions are in general consistent, there
 358 are clear differences among them. The most visible are (1) the concentration of three separated patches in model C that are not
 359 as clear in the other two models (i.e. one of them far from the coast and below 40 km depth, and another one to the east) which
 360 may be artificial to explain the data due to lack of regularization; none of them present in solutions A and B, and (2) the peak
 361 slip values that range between 20 and 25 cm. Moment magnitudes are also slightly different (i.e. 7.4 and 7.6 for models A
 362 and C, respectively). However, all three models coincide on the updip SSE penetration west of station CAYA, where our model
 363 has resolution higher than 60% up to a distance of 30 km west of that station. This region is of critical importance because it

364 extends along the NW-GGap, where recent onshore and offshore observations show that slow earthquake indeed happen there
365 in a particular way, and thus where the mechanical properties of the plate interface are different (Cruz-Atienza et al., 2020;
366 Plata-Martnez et al., 2020). Models B and C are remarkably different between stations ZIHP and CAYA, where the InSAR data
367 used for model B does not play a significant role. West of this region, model B predicts a very large shallow penetration of
368 the SSE across the mechanically stable zone where three M7+ earthquakes have taken place, the last in 2014 (see past rupture
369 areas)(UNAM, 2015). For this reason, model C, which is consistent with our model A, is the most plausible one for that zone.
370 Besides, our resolution close to the ZIHP station is higher than 60% as well. In conclusion, our preferred ELADIN solution has
371 the most reliable features of both previously published slip models.

372 **Conclusions**

373 We have introduced the ELADIN method, a new fault-slip inversion technique based on the adjoint elastostatic equations under
374 a constrained optimization framework. The method takes advantage of both the von Karman autocorrelation function to control
375 the problem regularization and the gradient projection method to impose physically-consistent slip restrictions (i.e. interplate
376 coupling smaller than any given value and rake angles consistent with the relative plate motion). To account for the data
377 uncertainty, the method weights the observations according to their individual covariance using the precision matrix. Synthetic
378 slip inversions from strongly perturbed data show that the model restitution across the plate interface is surprisingly high when
379 this uncertainty is taken into account (i.e. for both SSE and coupled interface regions). The ELADIN method thus allows
380 determining the aseismic slip on any 3D plate interface (or any fault surface) by simultaneously inverting slipping and coupled
381 fault areas with a spectral control of the problem solution that guaranties a given resolution criterion. We defined this criterion
382 by means of the mobile checkerboard restitution index (mcric), which allows determining fault regions where the resolution (i.e.
383 the slip restitution index) is high enough for a given von Karman autocorrelation length, L . This means that the inverted slip in
384 those regions is valid (to some desired extent) within the wavenumber bandwidth associated to the von Karman spectrum for
385 that L .

386 After performing a thorough resolution analysis of the study region, we inverted the 2006 Guerrero SSE. Our preferred slip
387 model obtained with the ELADIN method, for $L = 30\text{km}$, was compared with two previously published solutions and found
388 that it has the most reliable features of these two models. On one hand, our model is consistent with the solution of Cavali et al.
389 (2013) in that it places the maximum slip region above 40 km depth (i.e. downdip from stations CAYA and COYU), where
390 this solution is well constrained thanks to the InSAR data track. On the other, although all solutions predict the SSE shallow
391 penetration along a large part of the NW-GGap segment (west of CAYA), our model is closer to the solution of Radiguet et al.
392 (2011), where there is only GPS data. In this sense and considering also that to the east of station ZIHP are the rupture areas
393 of previous M7+ thrust earthquakes (i.e. a mechanically unstable zone), our SSE model is likely more realistic because it tends
394 to avoid that zone. Since resolution is unacceptable outside our confidence contours, we cannot confirm that the updip SSE

395 penetration between stations ZIHP and CAYA is reliable.

396 A systematic application of the ELADIN method has been recently done to invert recent data from the large set of GPSs shown
397 in Figure 1 (Cruz-Atienza et al., 2020), which has produced interesting results for the period 2016-2019, where three major
398 earthquakes and multiple SSEs occurred throughout the Mexican subduction zone.

399 **Acknowledgements**

400 We thank Mathilde Radiguet for providing the 2006 SSE data. The Somigliana tensor was computed in Miztli, UNAM cluster,
401 thanks to the CPU-hours assigned through the grant LANCAD-UNAM-DGTIC-312. SSE inversions were performed in the
402 Gaia supercomputing platform of the Institute of Geophysics at UNAM. This work was supported by UNAM-PAPIIT grants
403 IN113814 and IG100617, JICA-JST SATREPS-UNAM grant 15543611 and CONACyT grants 255308 and 6471.

404 **References**

- 405 Amey, R. M. J., Hooper, A., and Walters, R. J. (2018). A bayesian method for incorporating self-similarity into earthquake slip
406 inversions. *Journal of Geophysical Research: Solid Earth*, 123(7):6052–6071.
- 407 Askan, A., Akcelik, V., Bielak, J., and Ghattas, O. (2007). Full Waveform Inversion for Seismic Velocity and Anelastic Losses
408 in Heterogeneous Structures. *Bulletin of the Seismological Society of America*, 97(6):1990–2008.
- 409 Asnaashari, A., Brossier, R., Garambois, S., Audebert, F., Thore, P., and Virieux, J. (2013). Regularized seismic full waveform
410 inversion with prior model information. *Geophysics*, 78(2):R25–R36.
- 411 Bekaert, D. P. S., Hooper, A., and Wright, T. J. (2015). Reassessing the 2006 guerrero slow-slip event, mexico: Implications
412 for large earthquakes in the guerrero gap. *Journal of Geophysical Research: Solid Earth*, 120(2):1357–1375.
- 413 Calvetti, D., Morigi, S., Reichel, L., and Sgallari, F. (2000). Tikhonov regularization and the l-curve for large discrete ill-posed
414 problems. *Journal of computational and applied mathematics*, 123(1-2):423–446.
- 415 Campillo, M., Singh, S., Shapiro, N., Pacheco, J., and Herrmann, R. (1996). Crustal structure south of the mexican volcanic
416 belt, based on group velocity dispersion. *Geofisica Internacional*, 35(4):361–370.
- 417 Cavali, O., Pathier, E., Radiguet, M., Vergnolle, M., Cotte, N., Walpersdorf, A., Kostoglodov, V., and Cotton, F. (2013). Slow
418 slip event in the mexican subduction zone: Evidence of shallower slip in the guerrero seismic gap for the 2006 event revealed
419 by the joint inversion of insar and gps data. *Earth and Planetary Science Letters*, 367:5260.

- 420 Cruz-Atienza, V., Tago, J., Villafuerte, C., Wei, R., Garza-Girn, R., Domnguez, L., Kostoglodov, V., Nishimura, T., Franco, S.,
421 Real, J., Santoyo, M., Ito, Y., and Kazachkina, E. (2020). Short-term interaction between silent and devastating earthquakes
422 in mexico. Submitted to Science.
- 423 CruzAtienza, V. M., Ito, Y., Kostoglodov, V., Hjrleifsdttir, V., Iglesias, A., Tago, J., Cal, M., Real, J., Husker, A., Ide, S.,
424 Nishimura, T., Shinohara, M., MorteraGutierrez, C., Garca, S., and Kido, M. (2018). A Seismogeodetic Amphibious Network
425 in the Guerrero Seismic Gap, Mexico. Seismological Research Letters, 89(4):1435–1449.
- 426 Dragert, H., Wang, K., and James, T. S. (2001). A silent slip event on the deeper cascadia subduction interface. Science,
427 292(5521):1525–1528.
- 428 Fichtner, A., Bunge, H.-p., and Igel, H. (2006). The adjoint method in seismology: I. theory. Physics of the Earth and Planetary
429 Interiors, 157:86–104.
- 430 Fichtner, A., Kennett, B., Igel, H., and Bunge, H.-p. (2010). Full waveform tomography for radially anisotropic structure: New
431 insights into present and past states of the australasian upper mantle. Earth and Planetary Science Letters, 290:270–280.
- 432 Fukuda, J. and Johnson, K. M. (2008). A fully bayesian inversion for spatial distribution of fault slip with objective smoothing.
433 Bulletin of the Seismological Society of America, 98(3):1128–1146.
- 434 Gauthier, O., Virieux, J., and Tarantola, A. (1986). Two-dimensional nonlinear inversion of seismic waveforms: Numerical
435 results. Geophysics, 51(7):1341–1519.
- 436 Kostoglodov, V., Husker, A., Shapiro, N. M., Payero, J. S., Campillo, M., Cotte, N., and Clayton, R. (2010). The 2006 slow
437 slip event and nonvolcanic tremor in the mexican subduction zone. Geophysical Research Letters, 37(24).
- 438 Kostoglodov, V., Singh, S. K., Santiago, J. A., Franco, S. I., Larson, K. M., Lowry, A. R., and Bilham, R. (2003). A large silent
439 earthquake in the guerrero seismic gap, mexico. Geophysical Research Letters, 30(15).
- 440 Krischer, L., Fichtner, A., Boehm, C., and Igel, H. (2018). Automated large-scale full seismic waveform inversion for north
441 america and the north atlantic. Journal of Geophysical Research: Solid Earth, 123(7):5902–5928.
- 442 Mai, P. M. and Beroza, G. C. (2002). A spatial random field model to characterize complexity in earthquake slip. Journal of
443 Geophysical Research: Solid Earth, 107(B11):ESE 10–1–ESE 10–21.
- 444 McCaffrey, R., Qamar, A., King, R., Wells, R., Khazaradze, G., Williams, C., Stevens, C., Vollick, J., and Zwick, P. (2007).
445 Fault locking, block rotation and crustal deformation in the pacific northwest. Geophysical Journal International - GEOPHYS
446 J INT, 169:1315–1340.
- 447 Métivier, L. and Brossier, R. (2016). The seiscopes optimization toolbox: A large-scale nonlinear optimization library based on
448 reverse communicationthe seiscopes optimization toolbox. Geophysics, 81(2):F1–F15.

- 449 Minson, S. E., Simons, M., and Beck, J. L. (2013). Bayesian inversion for finite fault earthquake source models I theory and
450 algorithm. Geophysical Journal International, 194(3):1701–1726.
- 451 Miyazaki, S., Segall, P., McGuire, J. J., Kato, T., and Hatanaka, Y. (2006). Spatial and temporal evolution of stress and slip rate
452 during the 2000 tokai slow earthquake. Journal of Geophysical Research: Solid Earth, 111(B3).
- 453 Nishimura, T., Hirasawa, T., Miyazaki, S., Sagiya, T., Tada, T., Miura, S., and Tanaka, K. (2004). Temporal change of
454 interplate coupling in northeastern japan during 19952002 estimated from continuous gps observations. Geophysical Journal
455 International, 157(2):901–916.
- 456 Nocedal, J. and Wright, S. J. (2006). Numerical Optimization. Springer, 2nd edition.
- 457 Nocquet, J. (2018). Stochastic static fault slip inversion from geodetic data with non-negativity and bound constraints.
458 Geophysical Journal International, 214(1):366–385.
- 459 Nocquet, J., Villegas-Lanza, J., Chlieh, M., Mothes, P., Rolandone, F., Jarrin, P., Cisneros, D., Alvarado, A., Audin, L.,
460 Bondoux, F., Martin, X., Font, Y., Rgnier, M., Valle, M., Tran, T., Beauval, C., Maguia-Mendoza, J., Martinez, W., Tavera,
461 H., and Yepes, H. (2014). Motion of continental slivers and creeping subduction in the northern Andes. Nature Geoscience,
462 214(7).
- 463 Ozawa, S., Nishimura, T., Suito, H., Kobayashi, T., Tobita, M., and Imakiire, T. (2011). Coseismic and postseismic slip of the
464 2011 magnitude-9 tohoku-oki earthquake. Nature, 475(7356):373–376.
- 465 Plata-Martnez, R., S., I., Shinohara, M., Garca, E., Mizuno, N., Domnguez, L., Taira, T., Yamashita, Y., Toh, A., Yamada, T.,
466 Real, J., Husker, A., Cruz-Atienza, V., and Ito, Y. (2020). Shallow slow earthquakes and subducted bathymetry to decipher
467 devastating earthquakes in the guerrero seismic gap. Submitted to Science.
- 468 Radiguet, M., Cotton, F., Vergnolle, M., Campillo, M., Valette, B., Kostoglodov, V., and Cotte, N. (2011). Spatial and temporal
469 evolution of a long term slow slip event: the 2006 Guerrero Slow Slip Event. Geophys. J. Int., 184:816–828.
- 470 Radiguet, M., Cotton, F., Vergnolle, M., Campillo, M., Walpersdorf, A., Cotte, N., and Kostoglodov, V. (2012). Slow slip events
471 and strain accumulation in the Guerrero gap, Mexico. J. Geophys. Res., 117.
- 472 Sánchez-Reyes, H. S., Tago, J., Métivier, L., Cruz-Atienza, V., and Virieux, J. (2018). An evolutive linear kinematic source
473 inversion. Journal of Geophysical Research: Solid Earth, 123(6):4859–4885.
- 474 Savage, J. C. (1983). A dislocation model of strain accumulation and release at a subduction zone. Journal of Geophysical
475 Research: Solid Earth, 88(B6):4984–4996.
- 476 Simpson, R., Schulz, S., Dietz, L., and Burford, s. R. (1988). The response of creeping parts of the san andreas fault to
477 earthquakes on nearby faults: Two examples. pure and applied geophysics, 126(2-4):665–685.

- 478 Somala, S. N., Ampuero, J.-P., and Lapusta, N. (2018). Finite-fault source inversion using adjoint methods in 3-d heterogeneous
479 media. Geophysical Journal International, 214(1):402–420.
- 480 Tarantola, A. (1984). Inversion of seismic reflection data in the acoustic approximation. Geophysics, 49(8):1259–1266.
- 481 Tarantola, A. and Valette, B. (1982). Generalized nonlinear inverse problems solved using the least squares criterion. Reviews
482 of Geophysics, 20(2):219–232.
- 483 Tromp, J., Tape, C., and Liu, Q. (2005). Seismic tomography, adjoint methods, time reversal and banana-doughnut kernels.
484 Geophysical Journal International, 160(1):195–216.
- 485 UNAM, S. (2015). Papanao, mexico earthquake of 18 april 2014 (mw7.3). Geofisica Internacional, 54:363–386.
- 486 Vergnolle, M., Walpersdorf, A., Kostoglodov, V., Tregoning, P., Santiago, J., Cotte, N., and Franco, S. (2010). Slow slip events
487 in mexico revised from the processing of 11 year gps observations. Journal of Geophysical Research: Solid Earth, 115(B8).
- 488 Villafuerte, C. and Cruz-Atienza, V. M. (2017). Insights into the causal relationship between slow slip and tectonic tremor in
489 guerrero, mexico. Journal of Geophysical Research: Solid Earth, 122(8):6642–6656.
- 490 Wallace, L. M. and Beavan, J. (2010). Diverse slow slip behavior at the hikurangi subduction margin, new zealand. Journal of
491 Geophysical Research: Solid Earth, 115(B12).
- 492 Yabuki, T. and Matsu'Ura, M. (1992). Geodetic data inversion using a bayesian information criterion for spatial distribution of
493 fault slip. Geophysical Journal International, 109(2):363–375.

494 **A Gradient projection method: Cauchy point calculation**

495 The Cauchy point is an optimal state computed with a descent direction that respects the feasible solution region. We begin by
496 reformulating our inverse problem, eqs. (9-11), as the quadratic problem

$$\frac{1}{2} \underline{D}^T \underline{G} \underline{D} + \underline{c}^T \underline{D}, \quad (16)$$

497 subject to

$$D_i^{j,l} \leq (\underline{E} \underline{D})_i \leq D_i^{j,u}, \quad i \in \{p, c\} \wedge j \in \{\text{SSE, Coupling}\} \text{ regime}, \quad (17)$$

498 where

$$\underline{G} = \underline{F}^T \underline{T}^T \underline{C}_d^{-1} \underline{T} \underline{F} + \beta \underline{F}^T \underline{W}^T \underline{W} \underline{F}, \quad (18)$$

$$\underline{c} = - \left[\underline{U}_o^T \underline{C}_d^{-1} \underline{T} \underline{F} + \underline{D}_p^T \underline{W}^T \underline{W} \underline{F} \right]. \quad (19)$$

499 The gradient without considering the inequality constraint, eq. (17), is

$$\underline{g} = \underline{G} \underline{D} + \underline{c}, \quad (20)$$

500 First, we need to identify the step lengths for which each slip component reaches its bound along the direction $-\underline{g}$ and store
501 them in \bar{t} . Then, we eliminate duplicate and zero values of \bar{t} to obtain a sorted reduced set of breakpoints $\{t_1, t_2, \dots, t_l\}$ such
502 that $t_i < t_{i+1}$ for $i \in \{1, 2, \dots, l-1\}$. With this set, we construct a set of intervals like $\{[0, t_1], [t_1, t_2], \dots, [t_{l-1}, t_l]\}$. Suppose
503 that we have not found the minimizer up to the interval $[t_{j-1}, t_j]$, then we can model the slip along that interval as

$$\underline{D}(t) = \underline{D}(t_{j-1}) + (\Delta t) \underline{p}^{j-1}, \quad (21)$$

504 where

$$\Delta t = t - t_{j-1} \in [0, t_j - t_{j-1}], \quad (22)$$

$$\underline{p}_i^{j-1} = \begin{cases} -g_i & \text{if } t_{j-1} < \bar{t}_i, \\ 0 & \text{otherwise.} \end{cases} \quad (23)$$

505 If we substitute eq. (21) in the quadratic cost function (16), we leave it as a function of Δt

$$q(\Delta t) = \frac{1}{2} (\underline{D}(t_{j-1}) + (\Delta t) \underline{p}^{j-1})^T \underline{G} (\underline{D}(t_{j-1}) + (\Delta t) \underline{p}^{j-1}) + \underline{c}^T (\Delta t) \underline{p}^{j-1}, \quad (24)$$

506 which can be reformulated as

$$q(\Delta t) = f_{j-1} + g_{j-1}\Delta t + \frac{1}{2}h_{j-1}(\Delta t)^2, \quad (25)$$

507 where

$$f_{j-1} = \frac{1}{2}D(t_{j-1})^T \underline{\mathbf{G}} D(t_{j-1}) + \underline{\mathbf{c}}^T \underline{\mathbf{D}}(t_j - 1), \quad (26)$$

$$g_{j-1} = D(t_{j-1})^T \underline{\mathbf{G}} \underline{\mathbf{p}}^{j-1} + \underline{\mathbf{c}}^T \underline{\mathbf{p}}^{j-1}, \quad (27)$$

$$h_{j-1} = (\underline{\mathbf{p}}^{j-1})^T \underline{\mathbf{G}} \underline{\mathbf{p}}^{j-1}. \quad (28)$$

508 The solution of this problem is

$$\Delta t^* = -\frac{g_{j-1}}{h_{j-1}}. \quad (29)$$

509 Only one of the following three cases can occur

510 (i) If $g_{j-1} > 0$ the minimizer is at $\Delta t^* = 0$ with $t^* = t_{j-1}$ and $p^* = p_{j-1}$.

511 (ii) If $\Delta t^* \in [0, t_j - t_{j-1})$ the minimizer is in the interval with $t^* = t_{j-1}$ and $p^* = p_{j-1}$.

512 (iii) If $\Delta t^* > t_j - t_{j-1}$ then try the nex interval.

513 Once the optimal step has been found, Δt^* , the Cauchy point is evaluated as

$$\underline{\mathbf{D}}^c = \underline{\mathbf{D}}(t^*) + \Delta t^* \underline{\mathbf{p}}^*. \quad (30)$$

514 **B Gaussian slip inversions**

515 Figures S1 and S2 show the synthetic data inversions and restitution indexes with and without noise of the Gaussian-like pulses
516 shown in Figures 4A and 4B, respectively.

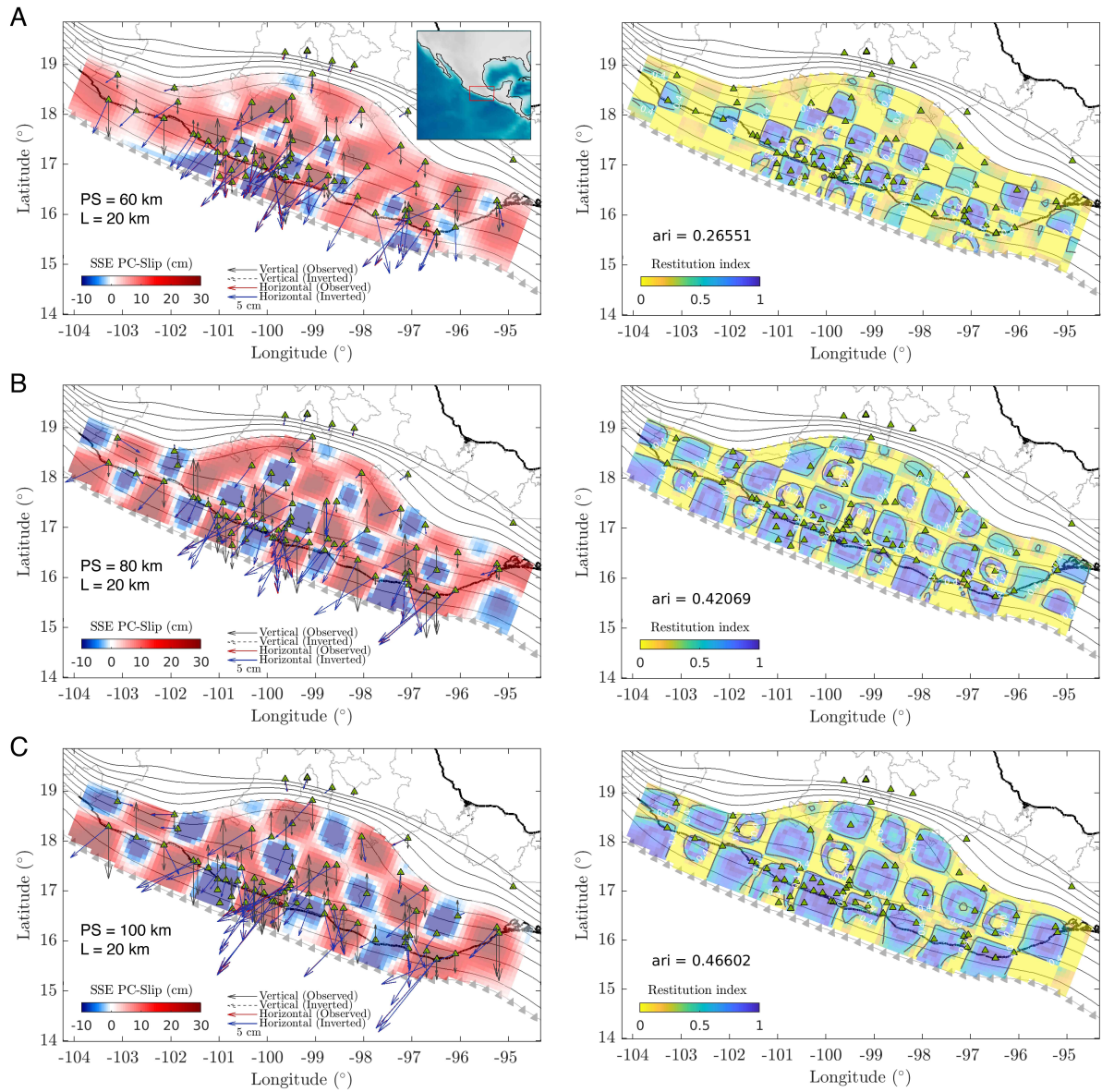


Figure 1: Checkerboard inversions for PS of (A) 60, (B) 80 and (C) 100 km, and correlation length, L, of 20 km. The inverted slip along with the surface displacement fits (left column) and the associated restitution index (right column) are displayed on the 3D plate interface (gray contours). Green triangles are the GPS stations.

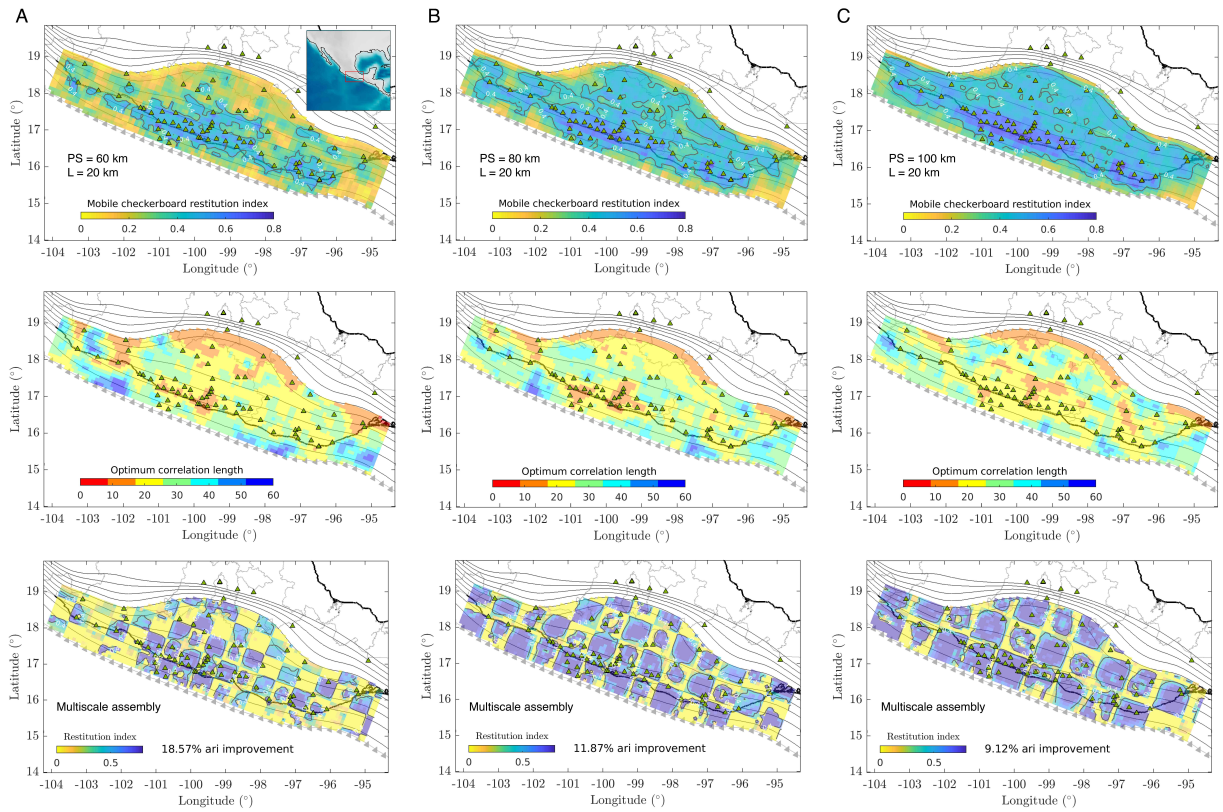


Figure 2: MOC tests for PS of (A) 60, (B) 80 and (C) 100 km and correlation length, L , of 20 km. Distributions of $mcri$ (first row), the optimum correlation length (second row) and the multiscale assembly of the restitution index (i.e. computed from the assembly of the best slip solutions for the CBs shown in Figure 1), all of them displayed on the 3D plate interface (gray contours). Green triangles are the GPS stations.

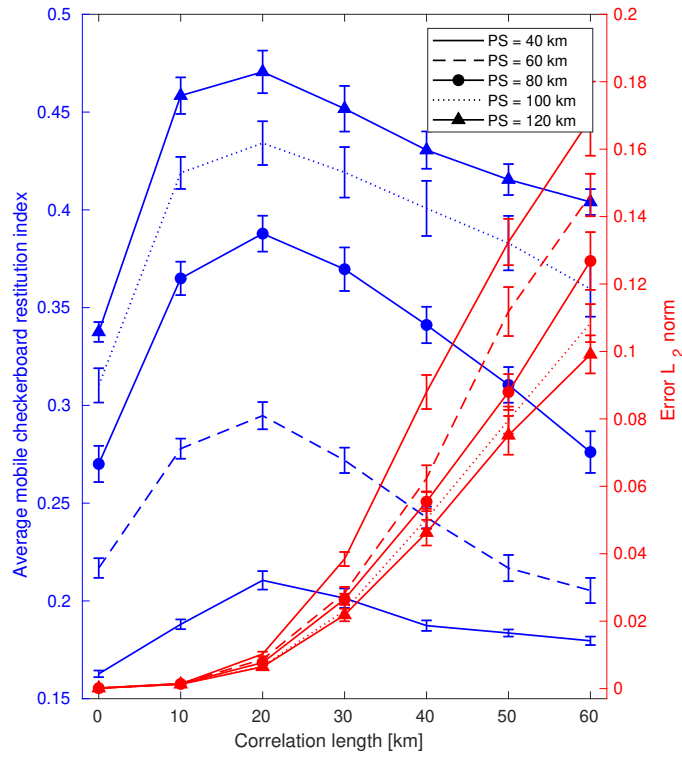


Figure 3: Results from all MOC tests in terms of the whole-interface average mcri (blue) and the average data-misfit error (red) as a function of the inversions correlation length L . PS (Patch Size) refers to the slip-patch characteristic length (i.e. the checkerboard unit size).

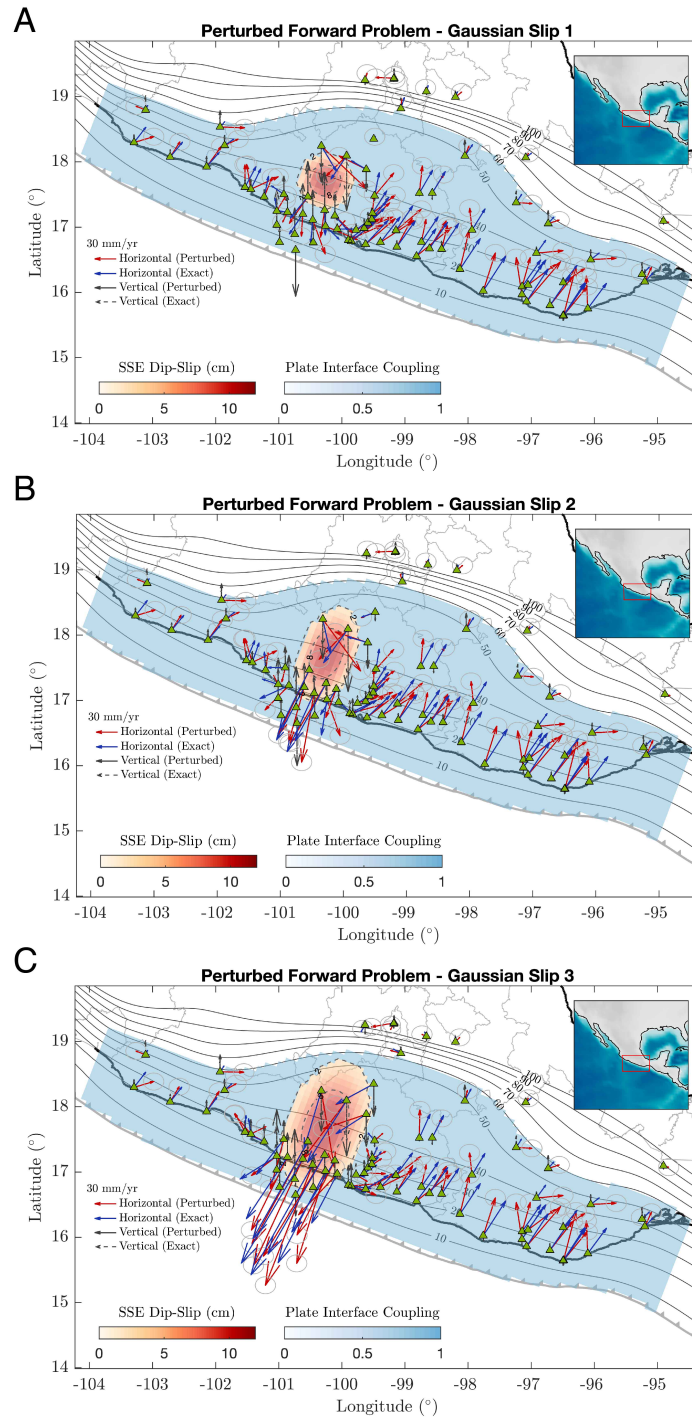


Figure 4: Slip models on the plate interface (background colors) and the associated model displacement predictions (arrows) for three Gaussian-like slip patches with different characteristic lengths. Blue and black-solid arrows show the exact surface displacements while red and black-dashed arrows show the same predictions but stochastically perturbed according to the normal distributions given by the data variance per component.

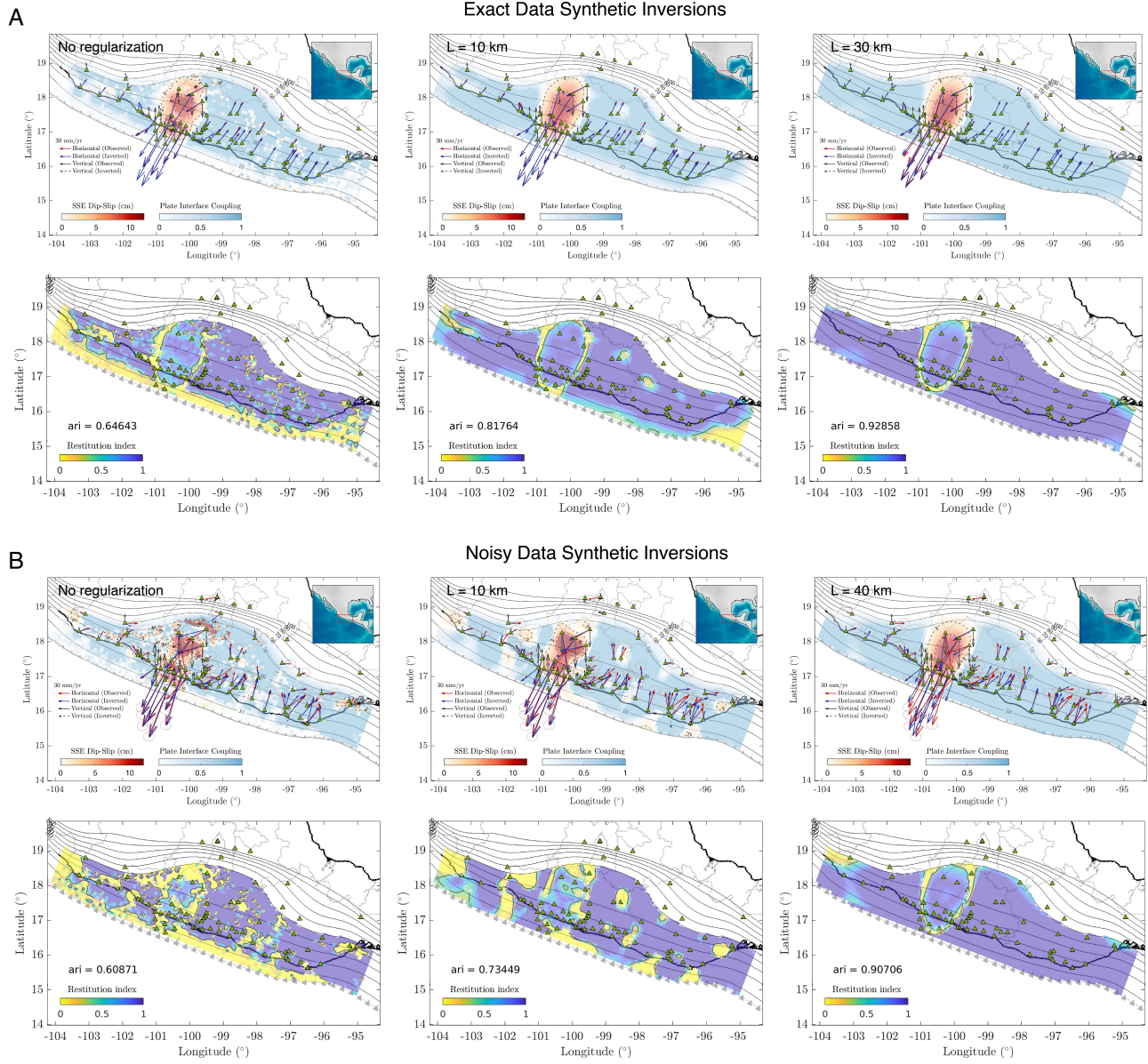


Figure 5: Synthetic inversion results for the slip model shown in Figure 4C from the exact target displacements (panel A) and from the perturbed (noisy) displacements (panel B). The second row of each panel shows the distribution of the restitution index over the plate interface without regularization and for different values of the correlation length, L .

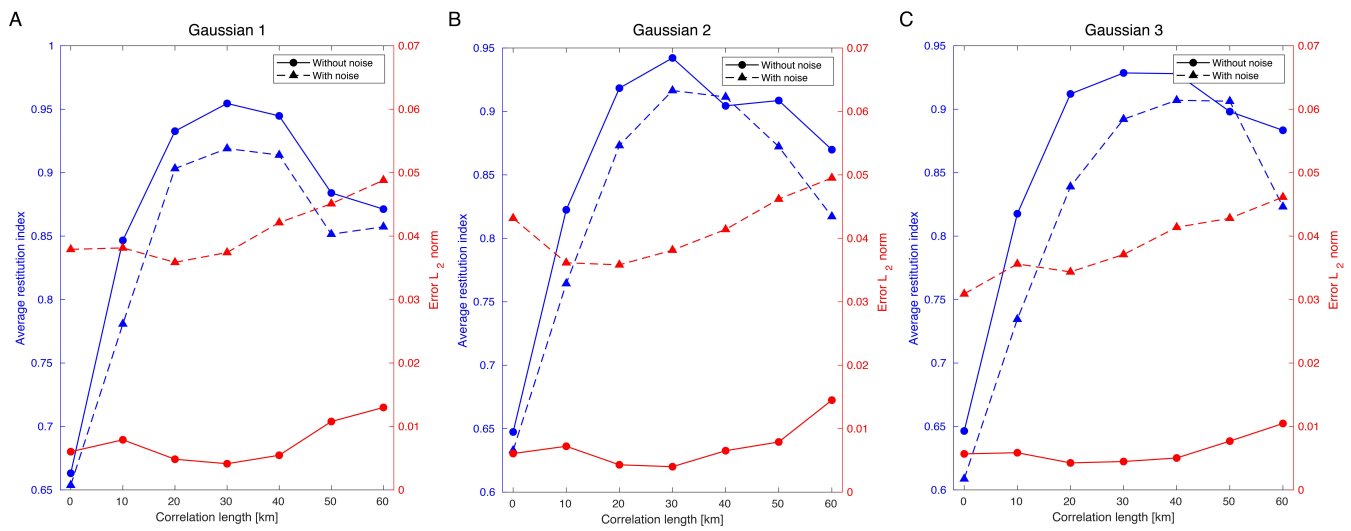


Figure 6: Synthetic inversion results for the three Gaussian-like slip functions shown in Figure 4 in terms of the whole-interface average restitution index (ari) and average data-misfit error (red) as a function of the inversions correlation length L . Solid lines correspond to the inversions using the exact data while dashed lines to the inversions with noisy data (see Figure 4). Notice that in all cases the maximum restitutions (ari) are above 0.9.

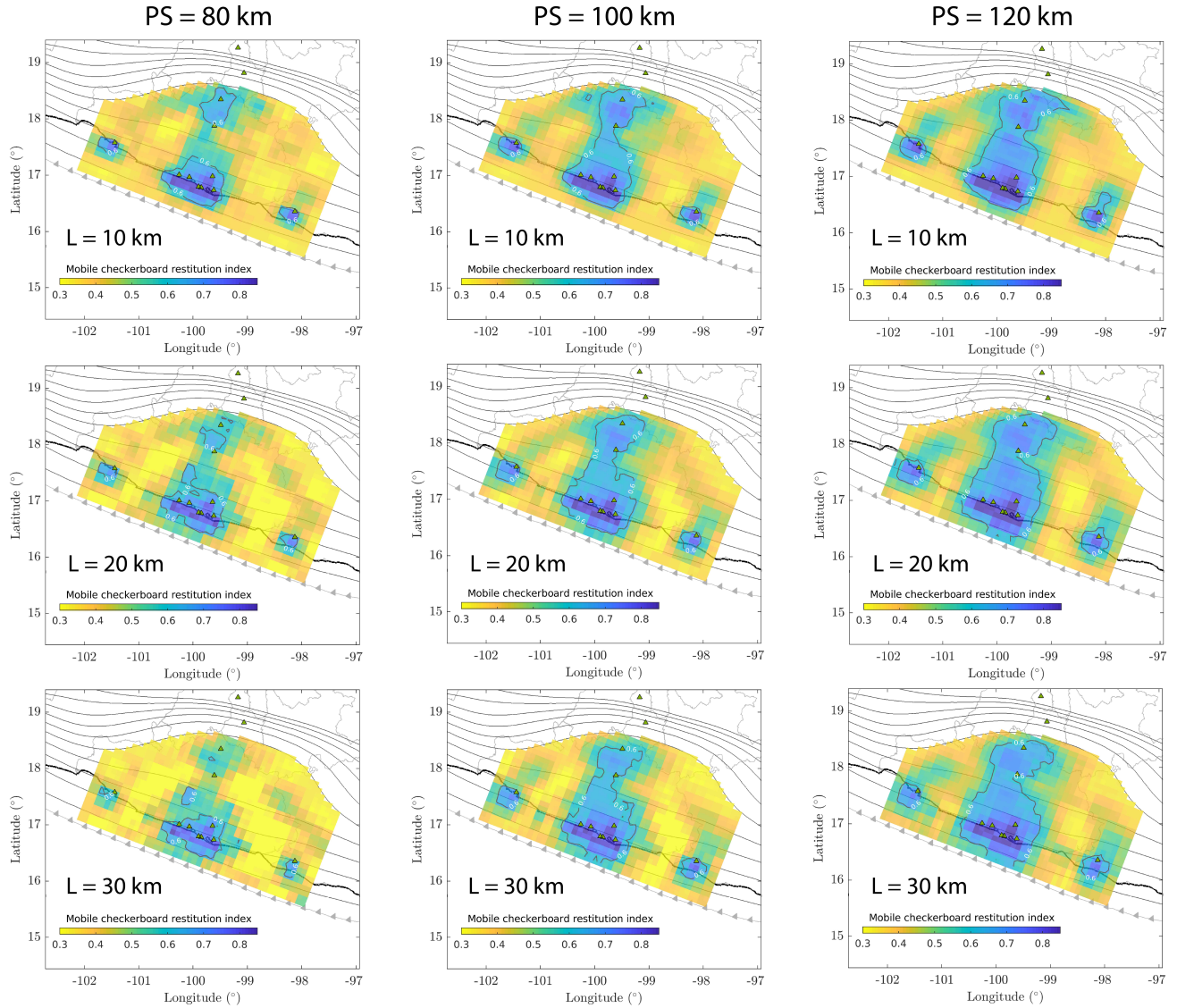


Figure 7: Plate interface distribution of the mobile checkerboard restitution index (mcri) for MOC tests corresponding to patch sizes (PS) of 80, 100 and 120 km and correlation lengths $L = 10, 20$ and 30 km for the 2006 SSE stations configuration. Black contours correspond to mcri values of 0.6 (i.e. slip resolution of 60%).

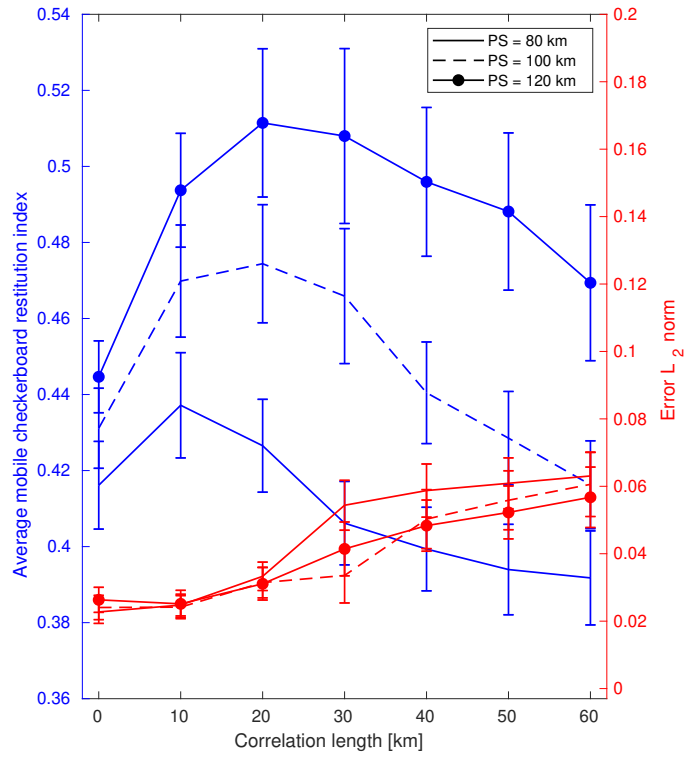


Figure 8: Results from all MOC tests for the 2006 SSE stations configuration in terms of the whole-interface average mcri (blue) and the average data-misfit error (red) as a function of the inversions correlation length L . PS (Patch Size) refers to the slip-patch characteristic length (i.e. the checkerboard unit size).

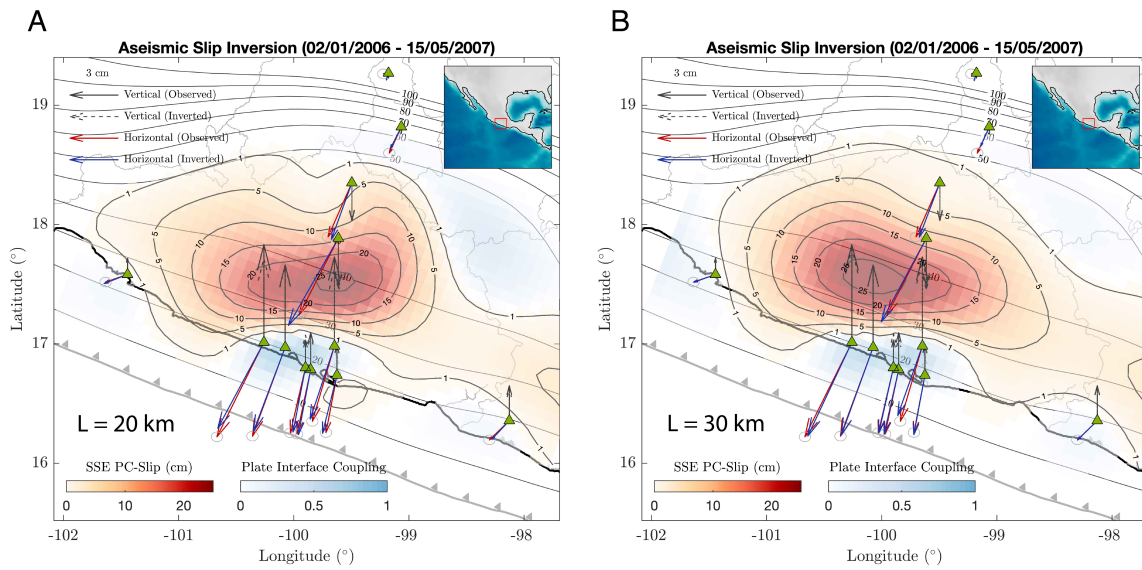


Figure 9: Aseismic slip inversions (in the plate convergence (PC) direction) of the 2006 Guerrero SSE for correlation lengths $L = 20$ km (A) and $L = 30$ km (B). The plate interface coupling is determined from the ratio between the back slip and the cumulative slip in the inverted period given a plate convergence rate of 6 cm/yr.

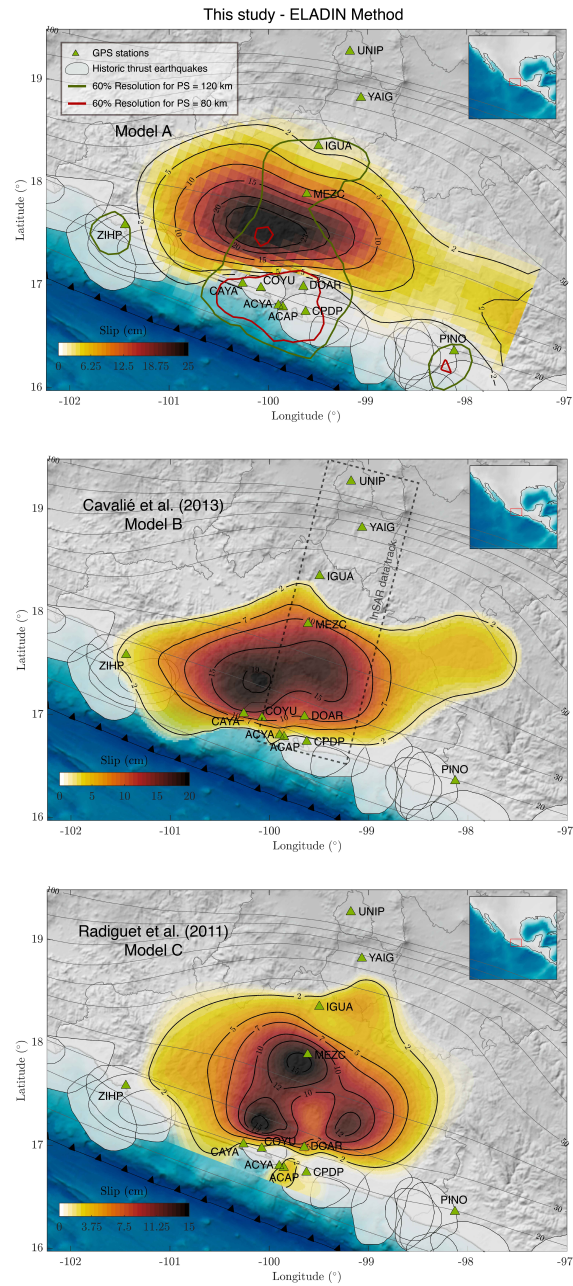


Figure 10: Comparison of our preferred solution (model A - for $L = 30$ km, Figure 9) with two previously published model for the 2006 Guerrero SSE, the one of Cavalié et al. (2013) (model B) and the one of Radiguet et al. (2011) (model C). 60% resolution contours for slip-patch (PS) characteristic lengths of 80 and 120 km are shown over model A.

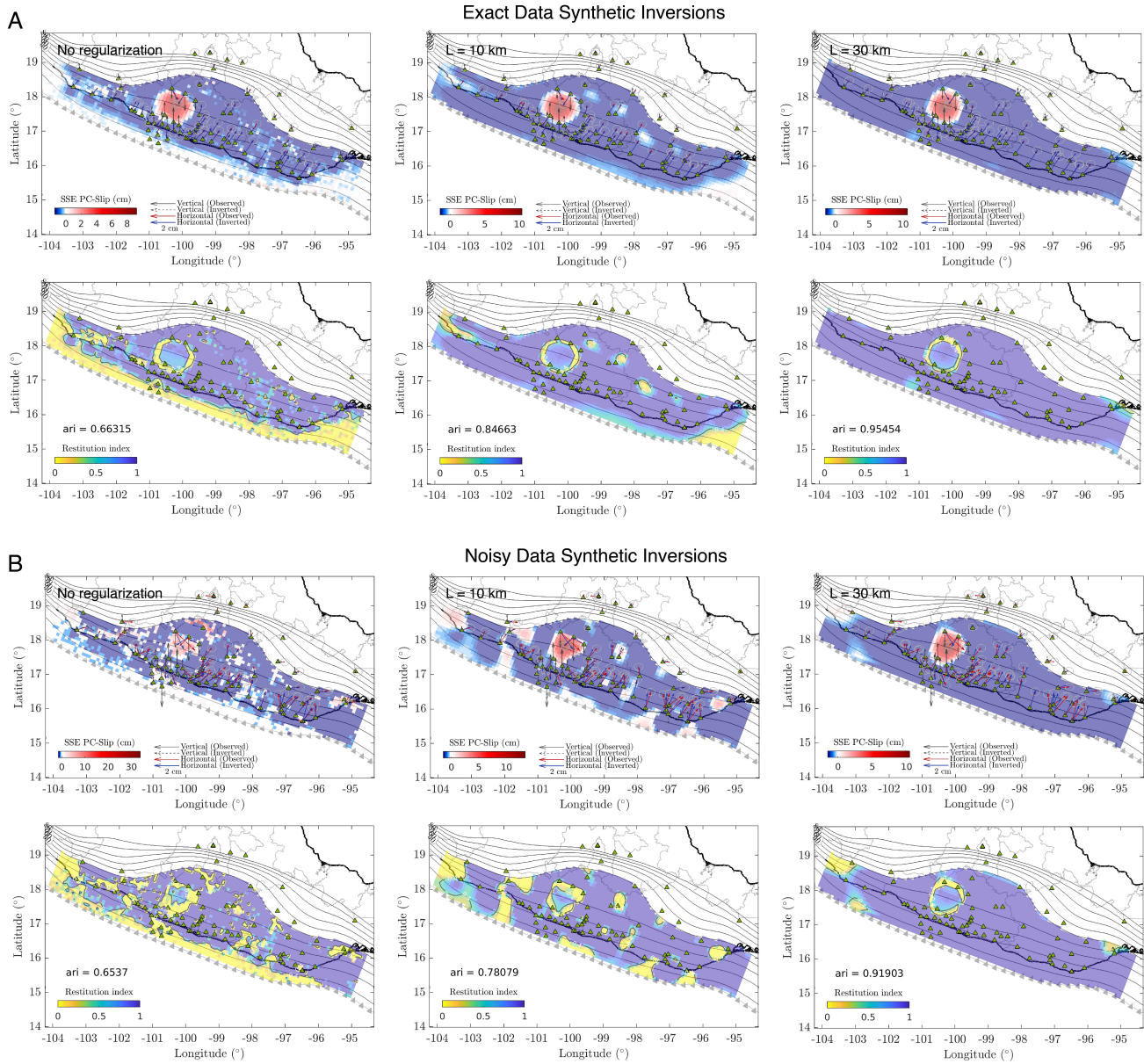


Figure S1: Synthetic inversion results for the Gaussian-like slip model shown in Figure 4A from the exact target displacements (panel A) and from the perturbed (noisy) displacements (panel B). The second row of each panel shows the distribution of the restitution index over the plate interface without regularization and for different values of the correlation length, L .

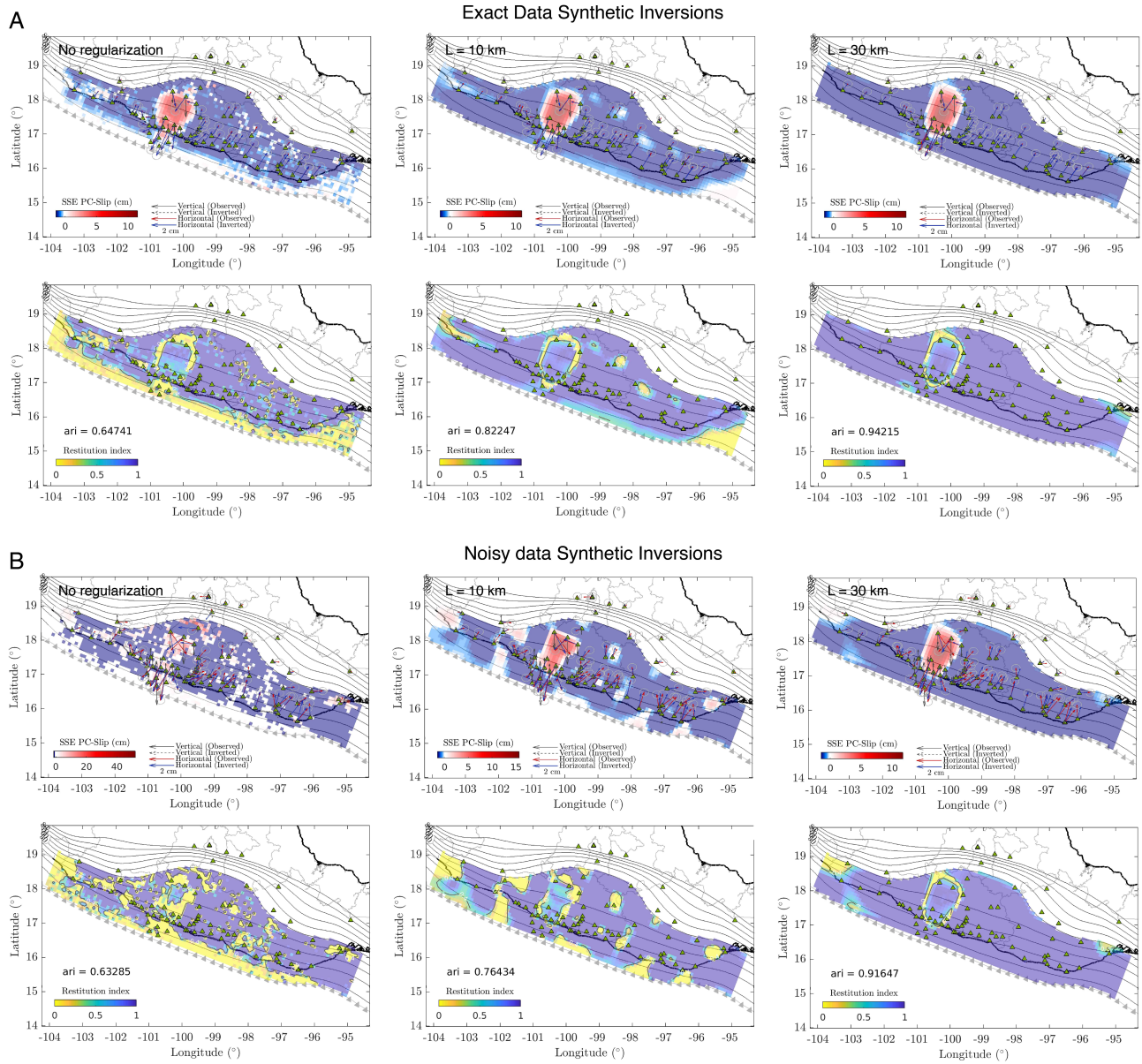


Figure S2: Synthetic inversion results for the Gaussian-like slip model shown in Figure 4B from the exact target displacements (panel A) and from the perturbed (noisy) displacements (panel B). The second row of each panel shows the distribution of the restitution index over the plate interface without regularization and for different values of the correlation length, L .